nature nanotechnology

LETTERS

https://doi.org/10.1038/s41565-019-0395-0

Bright sub-20-nm cathodoluminescent nanoprobes for electron microscopy

Maxim B. Prigozhin[1,15], Peter C. Maurer[1,15], Alexandra M. Courtis[2], Nian Liu[3,12], Michael D. Wisser[3], Chris Siefe[3], Bining Tian[4], Emory Chan[4], Guosheng Song[5,13], Stefan Fischer[3], Shaul Aloni[4], D. Frank Ogletree[4], Edward S. Barnard[4], Lydia-Marie Joubert[6,14], Jianghong Rao[5], A. Paul Alivisatos[2,7,8,9], Roger M. Macfarlane[10], Bruce E. Cohen[4], Yi Cui[3], Jennifer A. Dionne[3] and Steven Chu[1,11]*

Electron microscopy has been instrumental in our understanding of complex biological systems. Although electron microscopy reveals cellular morphology with nanoscale resolution, it does not provide information on the location of different types of proteins. An electron-microscopy-based bioimaging technology capable of localizing individual proteins and resolving protein–protein interactions with respect to cellular ultrastructure would provide important insights into the molecular biology of a cell. Here, we synthesize small lanthanide-doped nanoparticles and measure the absolute photon emission rate of individual nanoparticles resulting from a given electron excitation flux (cathodoluminescence). Our results suggest that the optimization of nanoparticle composition, synthesis protocols and electron imaging conditions can lead to sub-20-nm nanolabels that would enable high signal-to-noise localization of individual biomolecules within a cellular context. In ensemble measurements, these labels exhibit narrow spectra of nine distinct colours, so the imaging of biomolecules in a multicolour electron microscopy modality may be possible.

Nanoscale imaging of biomolecules in the context of cellular structures is essential for understanding how cells function. Although conventional electron microscopy is a powerful tool for the study of heavy-metal-stained cellular ultrastructure (that is, lipid membranes, cytoskeleton, chromatin and so on), it does not implicitly provide information about the location of specific biomolecules. Several approaches have been developed to visualize proteins in an electron microscopy micrograph, most notably tagging of target molecules with gold nanoparticles[1] and genetically encodable tags[2,3]. However, these electron-contrast-based techniques are inherently limited to imaging one protein species at a time, which prevents the study of protein–protein interactions and other complex processes. A related technology based on photo-precipitation of lanthanide ion complexes and energy-filtered transmission electron microscopy (TEM) has been reported[4]. However, this technology does not have single-molecule sensitivity and requires a distinctly addressable photosensitizer molecule for each lanthanide ion colour. In contrast, when electron microscopy is combined with optical super-resolution microscopy, different proteins can be tagged with spectrally distinguishable labels[5]. Although promising, such correlative light and electron microscopy methods require challenging sample preparation, suffer from systematic errors due to sample disruption at the nanoscale[5] and are susceptible to background luminescence[6].

An alternative approach to visualizing multiple proteins in an electron micrograph relies on tagging proteins with fluorescent molecules or nanoparticles, which, under excitation by an electron beam, emit light in a process known as cathodoluminescence (CL). In principle, this method allows for simultaneous acquisition of an electron micrograph and the locations of different proteins. However, organic dyes and fluorescent proteins disintegrate rapidly under electron exposure[7,8], and quantum dots are susceptible to bleaching in CL imaging[8]. Luminescent nanodiamonds and lanthanide-doped nanoparticles are more stable under electron beam irradiation and have been used for CL imaging, but only nanoparticles larger than ~40 nm (refs. [9–11]) or large aggregates have been reported to show a detectable CL signal[11]. The large size of these nanoparticles prevents specific protein labelling, which imposes a severe limitation on the use of these nanoparticles in biological experiments[12,13]. Even if such large nanoparticles can be synthesized so as not to form clusters, their size would not allow precise localization of the protein of interest with nanoscale resolution in an electron micrograph.

So far, it has remained an open question whether 'bright' cathodoluminescent nanoparticles can be synthesized on a sub-20-nm size scale, which would be small enough to potentially enable protein labelling in biological systems. Here, we report on the development of cathodoluminescent lanthanide-doped $NaGdF_4$ nanocrystals with a TEM nanoparticle full-width at half-maximum (FWHM) of 13.9 ± 5.0 nm (Fig. 1b and Supplementary Figs. 4 and 5). The size of the developed nanoprobes is comparable to that of quantum dots, gold nanoparticles and immunoglobulin antibodies, which are routinely used for immunolabelling in electron microscopy[14,15].

[1]Department of Physics, Stanford University, Stanford, CA, USA. [2]Department of Chemistry, University of California at Berkeley, Berkeley, CA, USA. [3]Department of Materials Science and Engineering, Stanford University, Stanford, CA, USA. [4]Molecular Foundry, Lawrence Berkeley National Laboratory, Berkeley, CA, USA. [5]Department of Radiology, Stanford University, Stanford, CA, USA. [6]CSIF Beckman Center, Stanford University, Stanford, CA, USA. [7]Materials Sciences Division, Lawrence Berkeley National Laboratory, Berkeley, CA, USA. [8]Department of Materials Science and Engineering, University of California, Berkeley, CA, USA. [9]Kavli Energy NanoScience Institute, Berkeley, CA, USA. [10]IBM Research – Almaden, San Jose, CA, USA. [11]Department of Molecular and Cellular Physiology, Stanford University, Stanford, CA, USA. [12]Present address: School of Chemical and Biomolecular Engineering, Georgia Institute of Technology, Atlanta, GA, USA. [13]Present address: State Key Laboratory of Chemo/Biosensing and Chemometrics, College of Chemistry and Chemical Engineering, Hunan University, Changsha, China. [14]Present address: EM Unit, Central Analytical Facilities, Stellenbosch University, Stellenbosch, South Africa. [15]These authors contributed equally: Maxim B. Prigozhin and Peter C. Maurer. *e-mail: schu@stanford.edu

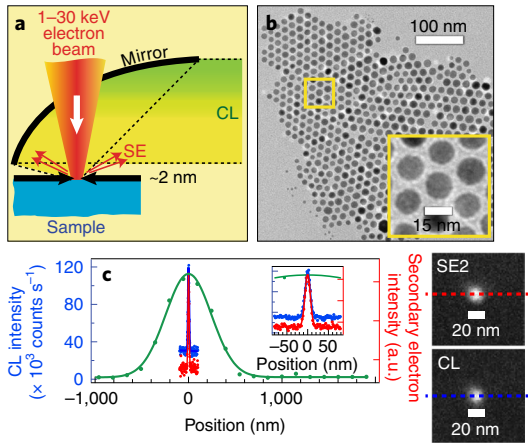

Fig. 1 | CL microscopy concept. a, Illustration of a CL instrument that uses an electron beam to induce emission of photons by nanoparticles (shown in **b**). CL emission is collected by a parabolic aluminium mirror and focused onto a photon-counting photomultiplier module. **b**, TEM image of $NaGdF_4$:5% Eu^{3+} nanoparticles. Inset, Magnified version of the region highlighted with a yellow square. **c**, Simultaneous SEM and CL imaging of the particle highlighted with green stars in Fig. 3b. Cross-sectional line profiles of SE (red, right axis) and CL (blue, left axis) scans of a single BF_4^--exchanged $NaGdF_4$:5% Eu^{3+} nanoparticle spin-coated on the Si substrate, imaged in parallel. The pixel pitch is 1.95 nm, the beam energy is 5 keV, the pixel dwell time is 2 ms and the beam current is ~400 pA. A cross-sectional line profile of a confocal light microscopy scan of a $NaYF_4$:18% Yb^{3+}, 2% Er^{3+} nanoparticle of similar size is shown in green (left axis). The excitation wavelength is 980 nm, and a water immersion objective with 1.27 numerical aperture is used. Inset, The same data, but with a zoomed-in *x* axis. Raw SE and CL data are shown on the right. All cross-sectional line profiles are fitted to a single-Gaussian model.

In this work, a scanning electron microscope (SEM) with a parabolic reflector was used to excite the CL of lanthanide-doped nanoparticles and image the CL signal onto a photomultiplying detector[16] (see Methods). In parallel with CL excitation and detection, the microscope also acquired the secondary electron (SE) signal from the same pixels registered in the CL channel (Fig. 1a). A key feature of CL imaging is its inherent nanoscale resolution. An electron beam with an energy of a few keV can be focused down to a few nanometres, although the resolution is usually limited by other factors such as CL excitation volume (see Supplementary Section 'Measurements and analysis of the electron beam sample interaction volume'), nanoparticle size and nanoparticle surface functionalization.

As an example of the capability of CL microscopy, a CL–SEM image of a single $NaGdF_4$:5% Eu^{3+} nanoparticle was acquired by detecting both the SE and CL signals in parallel (Fig. 1c). Cross-sectional line profiles of the SE (red) and CL (blue) signals from the same nanoparticle suggest that both electron microscopy and CL imaging can have comparable resolution, typical of SEM. In contrast, a confocal optical scan of an upconverting lanthanide-doped nanoparticle ($NaYF_4$:18% Yb^{3+}, 2% Er^{3+}) of similar size shows a diffraction-limited point spread function typical of optical far-field confocal microscopy. The specific nanoparticle shown in Fig. 1c was taken from a representative sample (see green star in Fig. 3b and green data point in Fig. 3d).

Previous work on lanthanide-doped nanoparticle synthesis has mainly focused on obtaining nanoparticle compositions that optimize the excitation and emission efficiency in optical upconversion[17], a process that is fundamentally different from CL excitation[18]. Therefore, an independent investigation of the CL brightness of rare earth nanoparticles as a function of their composition was required. Such optimization was achieved by synthesizing a series of $NaGdF_4$ and $NaYF_4$ nanoparticles of varying Eu^{3+} doping levels (see Methods) and characterizing their CL brightness at the single-nanoparticle level (see Methods). Nanoparticles were synthesized using a colloidal synthesis method as described in the Methods[19–22] (Supplementary Figs. 1–3). The as-synthesized nanoparticles were ligand-exchanged with nitrosonium tetrafluoroborate ($NOBF_4$) and dispersed in dimethylformamide (DMF) (see Methods)[23]. For CL–SEM imaging, multiple samples from the same synthesis run were prepared by spin-coating the dispersion of nanoparticles in DMF on a silicon substrate. The concentration of the nanoparticle solution used for spin-coating was adjusted so that at least three isolated nanoparticles could be found in an area of 1 μm^2. The samples were imaged in CL–SEM as described in the Methods.

Figure 2a,b shows sample CL–SEM images of $NaGdF_4$:5% Eu^{3+} nanoparticles (Fig. 3b, magenta arrow; Fig. 3d, magenta point). In a typical experiment, a 1 μm^2 field of view was imaged with a 1.95 nm pixel pitch (comparable to the typical electron beam size) and a pixel dwell time of 2 ms using a 5 keV electron beam with a current of ~400 pA (current density ~100 pA nm^{-2}; ~6.2×10^6 electrons s^{-1} $Å^{-2}$; dose of ~12.5×10^3 electrons $Å^{-2}$ within the 2 ms pixel dwell time). The SE image (Fig. 2a) was collected in parallel with the CL image (Fig. 2b). To extract the CL intensity and CL signal-to-noise ratio (CL SNR) for individual nanoparticles, a sub-region within the original 1 μm^2 field of view containing one or several individual nanoparticles was selected. Nanoparticle aggregates were deliberately excluded from the analysis. For the case when a single nanoparticle was selected, its raw image was fitted to a two-dimensional (2D) Gaussian function with a linearly sloped background. This fit was used to extract the CL intensity and SNR for each individual nanoparticle (see Methods). To compute the CL SNR, the CL signal was assumed to follow a Poisson distribution. This assumption was based on analysis of the background from repeated CL–SEM scans (Supplementary Section 'Background CL noise is described by Poisson statistics' and Supplementary Fig. 10). Because the ions that comprise rare-earth nanoparticles have high atomic numbers compared to the constituents of the biological tissue, a positive identification of a nanoparticle can be done using the SE or back-scattered electron signal. In this work, every $NaGdF_4$:5% Eu^{3+} nanoparticle was clearly seen on the Si substrate in the SE detection channel. Once a nanoparticle is identified in the electron imaging channel, CL counts are only required to identify the spectral identity of this nanoparticle, which relaxes the SNR requirements. (For further details, see Methods and Supplementary Section 'Single-particle signal-to-noise ratio', Supplementary Fig. 13 and 'Estimation of the number of observable colours and the required photon count rate'). However, as described in the sections 'Single-particle signal-to-noise ratio' and 'CL noise scaling of individual nanoparticles', the actual 'noise', as it is defined in this section, can be larger by up to a factor of two due to systematic effects such as astigmatism, charging and drift (see Supplementary Section 'CL noise scaling of individual nanoparticles' and Supplementary Fig. 11). Because of these effects, we conservatively define an individual nanoparticle to be observable in the CL channel if the CL SNR of this nanoparticle is greater than 10, instead of the CL SNR of ~2 that would be sufficient if the noise was purely Poissonian.

The pixel pitch of 1.95 nm is significantly smaller than the SEM nanoparticle FWHM of 21 ± 6 nm (Fig. 2d; 13.9 ± 5.0 nm TEM FWHM; Supplementary Figs. 4 and 5), leading to oversampling. An improvement in signal quality can be achieved by Fourier filtering. Figure 2c–e shows the CL intensity after Gaussian-filtering the image. In Fig. 2d, the CL counts per second and the CL SNR of all the individual nanoparticles from Fig. 2a,b are shown. CL intensity data in Fig. 2d are fit to a cubic curve (volumetric scaling, $FWHM^3$; see blue curve), and the CL SNR data are fit to an exponent of 3/2

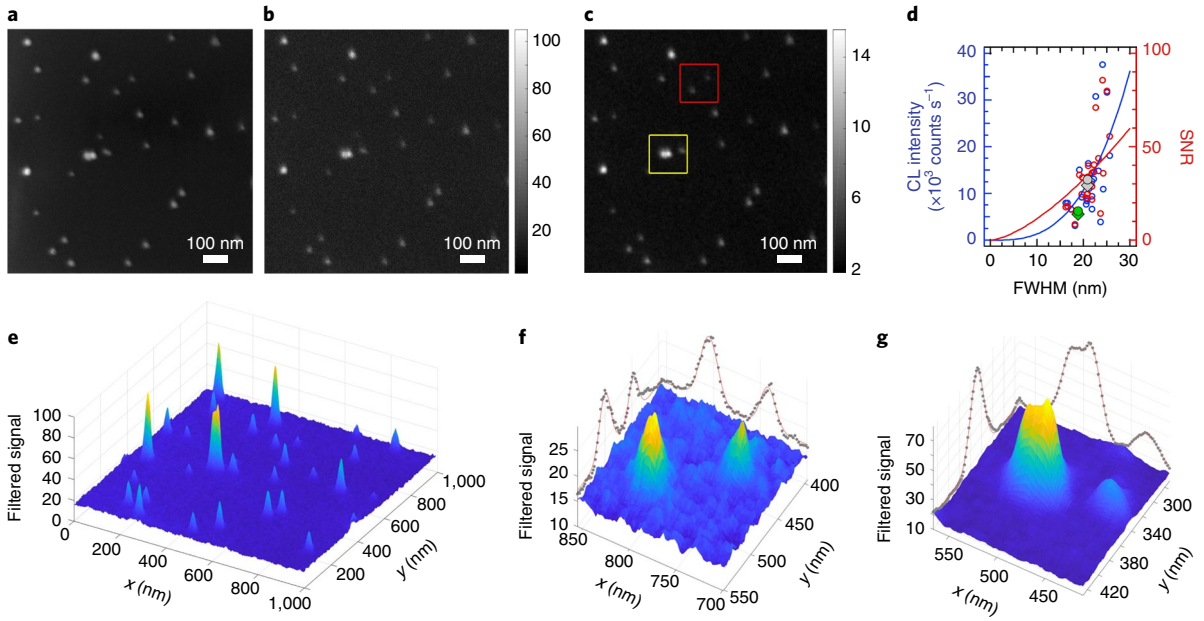

Fig. 2 | CL imaging of single $NaGdF_4$:5% Eu^{3+}. The nanoparticles were BF_4-exchanged and spin-coated on a Si substrate. **a**,**b**, Raw SE image (**a**) and corresponding CL signal (detected photons) (**b**). Images have an area of 1 μm², the pixel pitch is 1.95 nm, the beam energy is 5 keV, the pixel dwell time is 2 ms (8 min 44 s image acquisition time) and the beam current is ~400 pA. **c**, Fourier-filtered CL image of **b** using a Gaussian smoothing function of $\sigma = 7.16$ nm. **d**, CL intensity (blue, left axis) and CL SNR (red, right axis) for all the single nanoparticles from **a** and **b**, plotted as a function of the nanoparticle SEM FWHM (2.35σ) of the 2D Gaussian distribution fitted to each nanoparticle CL signal. (Note that the TEM diameter (13.9 ± 5.0 nm) is a more accurate measurement of the particle diameter than SEM, which can be skewed by charging and contamination; see Fig. 1b and Supplementary Fig. 4 for TEM data.) **e**, 3D representation of **c**. **f**,**g**, Images of the zoomed-in red (**f**) and yellow (**g**) regions in **c**. The data points for the nanoparticles in **f** are highlighted with diamonds (CL signal) and circles (CL SNR) in **d**. Grey corresponds to the brighter and green to the dimmer nanoparticle. A doublet of nanoparticles is shown in **g**. The dotted points on the sides of **f** and **g** correspond to a maximum intensity projection of the filtered CL signal. The red lines represent a guide to the eye (Gaussian fit).

(square-root scaling of the noise with respect to the signal; see red curve). The deviation of the data from the cubic fit indicates that the intensity does not follow a simple volumetric dependence with the SEM nanoparticle FWHM, in accordance with surface quenching reported for small optically excited nanoparticles[24]. Importantly, Fig. 2d illustrates that 13.9 ± 5.0 nm TEM FWHM nanoparticles can be observed in CL microscopy. Figure 2f,g depicts 3D visualizations of the CL signal of individual nanoparticles highlighted with red and yellow boxes in Fig. 2c, respectively. The data points for the nanoparticles in Fig. 2f are highlighted in Fig. 2d with diamonds (CL signal, left axis) and circles (CL SNR, right axis). The corresponding SEM scan in Fig. 2a proves that the CL emission originates from individual nanoparticles. For example, the dimmer particle in the red rectangle in Fig. 2c has a CL SNR of 15.7 and is clearly visible in the filtered CL image (Fig. 2f).

Despite the high CL intensity in certain samples, the CL emission of $NaGdF_4$:Eu^{3+} nanoparticles varied drastically between different experiments. Even on a single sample (that is, a single 5 × 5 mm Si wafer substrate), the CL signal fluctuated as a function of the imaging position (Fig. 3a and Supplementary Figs. 16–22). Similar sample preparation also resulted in a large variation in signal, even if these samples were prepared from the same nanoparticle stock solution (Fig. 3b). Finally, particles that were synthesized under nominally identical conditions resulted in dramatically different CL emission rates (Fig. 3c). In the field of view (1 μm²) that contains the nanoparticles with the largest CL emission rate (position 5 in Fig. 3a; Supplementary Fig. 21) an average CL signal of $(7.1 \pm 2.2) \times 10^5$ counts s^{-1} was observed, but in other cases (for example, position 7 in Fig. 3a; Supplementary Fig. 23) the nanoparticles imaged by the CL-SEM were barely detectable in the CL channel. Supplementary Table 1 tabulates the number of SEM detected particles, and the number and fraction of nanoparticles with CL SNR > 10. The high variability of the CL signal for $NaGdF_4$:Eu^{3+} nanoparticles may originate from material-specific or synthesis-specific defects that lead to quenching of the luminescence. Such quenching can be caused, for example, by electron beam damage of the surrounding organic material or the nanoparticle itself[25]. The CL brightness of the $NaGdF_4$ nanoparticles as a function of Eu^{3+} doping level was also investigated (Fig. 3d). $NaGdF_4$ doped with Er^{3+} at various doping levels showed no detectable CL luminescence at the single-nanoparticle level (Supplementary Fig. 24a). Notably, the large variability in the CL brightness of individual $NaGdF_4$:Eu^{3+} nanoparticles was masked in ensemble CL measurements (Supplementary Fig. 26). This observation highlights the importance of single-nanoparticle CL measurements. In addition, the CL brightness of ~35 nm SEM FWHM $NaYF_4$ nanoparticles (Supplementary Figs. 6 and 7) doped with Eu^{3+} (Supplementary Fig. 25) and with Er^{3+} (Supplementary Fig. 24b) was more consistent from sample to sample compared to the $NaGdF_4$ nanoparticles. Further CL nanoprobe development is needed to achieve sub-20-nm nanoparticles with consistently high CL luminescence required for biological cell imaging.

Lanthanide ions have rich energy level diagrams with 4*f*-to-4*f* transitions that give rise to emission spectra that are characteristic of each individual lanthanide ion. Figure 4 shows ensemble CL spectra obtained for nine different types of $NaGdF_4$ nanoparticles doped with Eu^{3+}, Er^{3+}, Ho^{3+}, Tb^{3+}, Sm^{3+}, Dy^{3+}, Nd^{3+}, Tm^{3+} and Yb^{3+} ions (see Supplementary Fig. 6 for TEM images of $NaYF_4$ nanoparticles and Supplementary Fig. 27 for the CL spectra of $NaYF_4$ nanoparticles). The Er^{3+} doping was at 20%, while all other

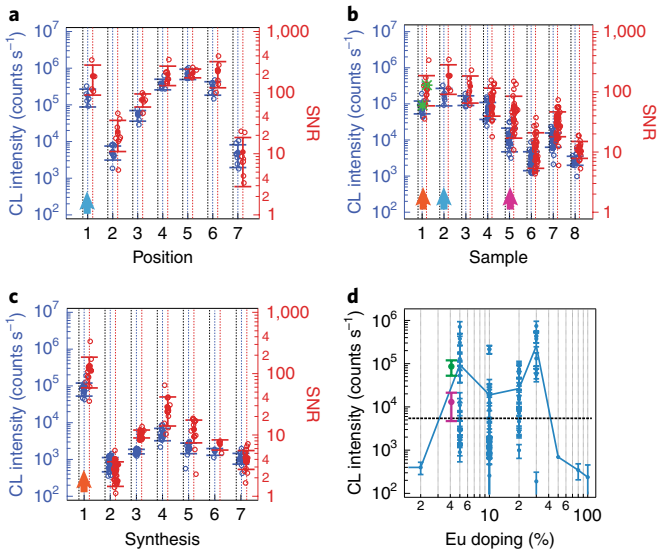

Fig. 3 | Variability of CL brightness and SNR. In all experiments, $NaGdF_4$:5% Eu^{3+} nanoparticles were BF_4^--exchanged and spin-coated on a Si substrate. **a**–**c**, CL variability and SNR are shown in **a** for the same sample (sample 2 in **b**) of the brightest synthesis run (synthesis 1 in **c**), in **b** for synthesis 1 but for a different sample preparation, and in **c** across different synthesis runs. Identical samples are marked with two blue arrows in **a** and **b** and with two orange arrows in **b** and **c**. The data used in Fig. 1c are highlighted in **b** with green stars and in **d** with a green data point (sample average). The data from Fig. 2 are highlighted with a magenta arrow in **b** and a magenta data point in **d**. Open circles represent the brightness (Gaussian amplitude) in counts per second (blue, left *y* axis) and the respective CL SNR (red, right *y* axis) for individual nanoparticles. Filled circles represent the corresponding average values. **d**, Average single nanoparticle brightness (each point represents a 1 μm^2 field of view) as a function of Eu^{3+} doping. Green and magenta data points represent data used in Fig. 1c and Fig. 2 (data points are offset to the left for visibility and correspond to 5% Eu^{3+}). The data include all measured samples (including different syntheses, different samples but the same synthesis, and different regions of the same sample). The solid blue line represents an average of intensities for each Eu^{3+} doping. The black horizontal dashed line represents the average noise level from **a**–**c** (5,449 counts s^{-1}) to illustrate the marginal CL intensity. All error bars correspond to one standard deviation.

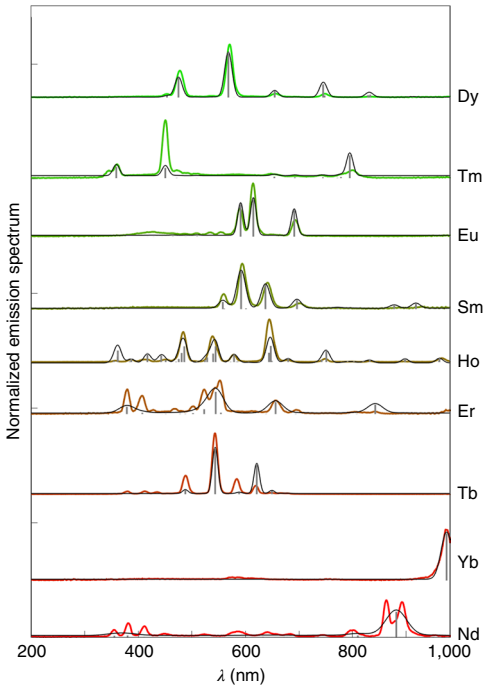

Fig. 4 | Multicolour imaging of lanthanide-based nanoprobes. a, Emission spectra of ensemble samples of *n*-hexane-washed $NaGdF_4$ (solid coloured lines) nanoparticles doped with different lanthanide ions (20% doping for Er^{3+}; 15% doping for the others) dropcast on a Si substrate. The data were acquired at 5 keV electron beam energy and corrected for spectrometer efficiency. Grey bars correspond to the Judd–Ofelt calculations (see Methods section 'Simulations of nanoparticle spectra' and Supplementary Fig. 31). Grey lines correspond to fitted spectra using linewidth as the only fitting parameter.

lanthanide ions were doped at 15%. All the spectra were acquired from films of *n*-hexane-washed nanoparticles using a JEOL JXA-8230 SuperProbe instrument (beam energy of 5 keV; probe current ~0.13 pA nm^{-2}, ~8×10^3 electrons s^{-1} Å^{-2}; see Methods). In addition, doping with Ce^{3+} and Pr^{3+}, and Gd^{3+} alone, was investigated but did not yield sharp spectra (see Supplementary Fig. 30 for the spectra of Ce^{3+}, Pr^{3+} and Gd^{3+}).

The narrow emission lines (21 ± 11 nm FWHM of spectral peaks) of lanthanide-doped nanoparticles and their invariance with respect to the host lattice are indicative of atom-like 4*f*-to-4*f* inner-shell transitions in lanthanide ions. The intensities of the transitions among these low-lying 4*f* states in lanthanide ions can be qualitatively described by Judd–Ofelt theory[26,27]. Figure 4 compares the experimental spectra to Judd–Ofelt theory[26,27] (Supplementary Section 'Simulations of nanoparticle spectra' and Supplementary Fig. 31). Differences in the oscillator strength of individual transitions probably arise because the Judd–Ofelt parameters often relied on rates extracted from different host lattices[28].

This work explores small sub-20-nm lanthanide-doped nanoparticles as prospective nanoscale labels for multicolour electron microscopy because of their potentially high photon count rate, sharp emission spectra and tunable size. The size of lanthanide-doped nanoparticles presented here is comparable to that of the quantum dots that are commonly used as luminescent labels in optical imaging[15], and only slightly larger than the gold nanoparticles used in electron microscopy[14]. This substantial reduction in nanoparticle size compared to the previously reported cathodoluminescent nanoparticles is a significant improvement because nanoparticles on the order of 10–20 nm in diameter are required for efficient biomolecular targeting and subsequent nanoscale localization of the molecules of interest in CL microscopy. A further reduction in size may be achieved by engineering core–shell structures that eliminate the adverse effects of the nanoparticle surface[29,30].

Furthermore, the long excited-state lifetimes of rare-earth nanoparticles[31] enable time-gated measurements that eliminate the CL background from the biological substrate[32] (Supplementary Fig. 29) and would allow the imaging of even smaller nanoparticles that have a lower CL intensity but are more suitable for targeted protein labelling and penetration into tissue samples[13]. Although the focus of the work presented here is on the development of bright cathodoluminescent nanoparticles, the CL background from potential biological substrates needs to be taken into account when designing optimal CL nanoprobes. Background-free measurements would make the detection of a few photons sufficient to successfully assign the nanoparticle colour (Supplementary Section 'Estimation of number of observable colours and required photon count rate'), potentially opening a path to ultrasmall labels for multicolour biological electron microscopy.

A better SNR can be achieved if the electron interaction volume is matched to the nanoparticle size (for a 15–20 nm diameter nanoparticle this corresponds to 0.75–1 keV electron landing energies; Supplementary Section 'Measurements and analysis of the electron beam sample interaction volume'). Theoretical analysis of inelastic scattering suggests that for a 15–20 nm diameter nanoparticle, the electron interaction volume would match the nanoparticle dimensions at the electron landing energy of 0.75–1 keV (Supplementary Fig. 16). In addition, this local excitation would also minimize the background from excitation by back-scattered electrons and SE in the substrate (Supplementary Figs. 14–15). The imaging energy of ~1 keV is also an optimal trade-off between the back-scattered electron contrast and the axial resolution in biological SEM[33]. In the future, rapid nanoparticle localization in the electron detection channel may allow each nanoparticle to be identified individually, significantly reducing the image acquisition time and electron dosage. Combining CL microscopy with the new multi-beam SEMs is expected to further increase the imaging speed.

Finally, the next generation of our experiment will focus on optimization of the synthesis parameters for the other lanthanide ions (that is, Ho^{3+}, Tb^{3+}, Sm^{3+}, Dy^{3+}, Nd^{3+}, Tm^{3+} and Yb^{3+}). Such an optimization, combined with a new multicolour CL imaging system, which enables simultaneous detection of multiple spectral components, may open the door to true multicolour imaging at the single-nanoparticle level. The potentially large photon count rate of individual nanoparticles (that is, $NaGdF_4$:5% Eu^{3+}) combined with the distinct spectra obtained in ensemble measurements suggest that up to nine different colours with 10–20 nm spatial resolution could be achieved (Supplementary Section 'Estimation of the number of observable colours and the required photon count rate' and Supplementary Fig. 28)[34]. A further increase in the number of colours may be achieved by co-doping nanoparticles with multiple lanthanide ions and detecting an emission spectrum characteristic of the exact particle composition[28]. Incidentally, another benefit of using low beam energy in CL imaging lies in the imaging of several nanoprobes of different colours, because the spectral identification would be compromised if stray electrons were able to excite neighbouring nanoparticles (Supplementary Section 'Measurements and analysis of the electron beam sample interaction volume').

Although reliable multicolour CL imaging at the single-nanoparticle level and in biological tissue remains to be demonstrated, our findings will motivate future work in this direction. Optimal multicolour imaging combined with advances in particle functionalization and labelling[35] could allow visualization of the locations of different proteins with respect to the cellular ultrastructure (organelles, vesicles, nucleic acids and other nanostructures). Protein-specific localization in the context of ~5 nm cell ultrastructure could have a significant impact on our understanding of the molecular architecture of the cell. Similarly, combining multicolour CL imaging with in situ serial-block-face SEM[36] or focused-ion-beam SEM[37] will permit full 3D reconstruction of entire tissue sections[37,38], while providing simultaneous nanoscale protein localization. Such biospecific volumetric electron imaging would enable the visualization of different cell types within heterogeneous tissue sections and shed light on the organization of complex systems such as the heart[39], the brain[38] or cancerous tissue[40].

Online content

Any methods, additional references, Nature Research reporting summaries, source data, statements of data availability and associated accession codes are available at https://doi.org/10.1038/s41565-019-0395-0.

Received: 23 May 2018; Accepted: 28 January 2019;
Published online: 04 March 2019

References

1. Roth, J., Bendayan, M. & Orci, L. Ultrastructural localization of intracellular antigens by the use of protein A–gold complex. *J. Histochem. Cytochem.* **26**, 1074–1081 (1978).
2. Martell, J. D. et al. Engineered ascorbate peroxidase as a genetically encoded reporter for electron microscopy. *Nat. Biotechnol.* **30**, 1143–1148 (2012).
3. Lam, S. S. et al. Directed evolution of APEX2 for electron microscopy and proximity labeling. *Nat. Methods* **12**, 51–54 (2015).
4. Adams, S. R. et al. Multicolor electron microscopy for simultaneous visualization of multiple molecular species. *Cell Chem. Biol.* **23**, 1417–1427 (2016).
5. Sochacki, Ka, Shtengel, G., van Engelenburg, S. B., Hess, H. F. & Taraska, J. W. Correlative super-resolution fluorescence and metal-replica transmission electron microscopy. *Nat. Methods* **11**, 305–308 (2014).
6. Carter, S. D. et al. Distinguishing signal from autofluorescence in cryogenic correlated light and electron microscopy of mammalian cells. *J. Struct. Biol.* **201**, 15–25 (2018).
7. Fisher, P. J., Wessels, W. S., Dietz, A. B. & Prendergast, F. G. Enhanced biological cathodoluminescence. *Opt. Commun.* **281**, 1901–1908 (2008).
8. Mahfoud, Z. et al. Cathodoluminescence in a scanning transmission electron microscope: a nanometer-scale counterpart of photoluminescence for the study of II–VI quantum dots. *J. Phys. Chem. Lett.* **4**, 4090–4094 (2013).
9. Zhang, H., Glenn, D. R., Schalek, R., Lichtman, J. W. & Walsworth, R. L. Efficiency of cathodoluminescence emission by nitrogen-vacancy color centers in nanodiamonds. *Small* **13**, 1700543 (2017).
10. Glenn, D. R. et al. Correlative light and electron microscopy using cathodoluminescence from nanoparticles with distinguishable colours. *Sci. Rep.* **2**, 1–6 (2012).
11. Niioka, H. et al. Multicolor cathodoluminescence microscopy for biological imaging with nanophosphors. *Appl. Phys. Express* **4**, 2402 (2011).
12. Cai, E. et al. Stable small quantum dots for synaptic receptor tracking on live neurons. *Angew. Chem. Int. Ed.* **53**, 12484–12488 (2014).
13. Yokota, S. Effect of particle size on labeling density for catalase in protein A–gold immunocytochemistry. *J. Histochem. Cytochem.* **36**, 107–109 (1988).
14. Kijanka, M. et al. A novel immuno-gold labeling protocol for nanobody-based detection of HER2 in breast cancer cells using immuno-electron microscopy. *J. Struct. Biol.* **199**, 1–11 (2017).
15. Giepmans, B. N. G., Deerinck, T. J., Smarr, B. L., Jones, Y. Z. & Ellisman, M. H. Correlated light and electron microscopic imaging of multiple endogenous proteins using quantum dots. *Nat. Methods* **2**, 743–749 (2005).
16. Bischak, C. G. et al. Cathodoluminescence-activated nanoimaging: noninvasive near-field optical microscopy in an electron microscope. *Nano Lett.* **15**, 3383–3390 (2015).
17. Feng, W., Zhu, X. & Li, F. Recent advances in the optimization and functionalization of upconversion nanomaterials for in vivo bioapplications. *NPG Asia Mater.* **5**, e75–15 (2013).
18. García De Abajo, F. J. Optical excitations in electron microscopy. *Rev. Mod. Phys.* **82**, 209–275 (2010).
19. Wang, F., Deng, R. & Liu, X. Preparation of core–shell $NaGdF_4$ nanoparticles doped with luminescent lanthanide ions to be used as upconversion-based probes. *Nat. Protoc.* **9**, 1634–1644 (2014).
20. Liu, Q., Feng, W., Yang, T., Yi, T. & Li, F. Upconversion luminescence imaging of cells and small animals. *Nat. Protoc.* **8**, 2033–2044 (2013).
21. Li, Z. & Zhang, Y. An efficient and user-friendly method for the synthesis of hexagonal-phase $NaYF_4$:Yb, Er/Tm nanocrystals with controllable shape and upconversion fluorescence. *Nanotechnology* **19**, 345606 (2008).
22. Ostrowski, A. D. et al. Controlled synthesis and single-particle imaging of bright, sub-10-nm lanthanide-doped upconverting nanocrystals. *ACS Nano* **6**, 2686–2692 (2012).
23. Dong, A. et al. A generalized ligand-exchange strategy enabling sequential surface functionalization of colloidal nanocrystals. *J. Am. Chem. Soc.* **133**, 998–1006 (2011).
24. Gargas, D. J. et al. Engineering bright sub-10-nm upconverting nanocrystals for single-molecule imaging. *Nat. Nanotechnol.* **9**, 300–305 (2014).
25. Feng, W., Sun, L. D., Zhang, Y. W. & Yan, C. H. Solid-to-hollow single-particle manipulation of a self-assembled luminescent $NaYF_4$:Yb,Er nanocrystal monolayer by electron-beam lithography. *Small* **5**, 2057–2060 (2009).
26. Judd, B. R. Optical absorption intensities of rare-earth ions. *Phys. Rev.* **127**, 750–761 (1962).
27. Ofelt, G. S. Intensities of crystal spectra of rare-earth ions. *J. Chem. Phys.* **37**, 511–520 (1962).
28. Chan, E. M. Combinatorial approaches for developing upconverting nanomaterials: high-throughput screening, modeling, and applications. *Chem. Soc. Rev.* **44**, 1653–1679 (2015).
29. Fischer, S., Johnson, N. J. J., Pichaandi, J., Goldschmidt, J. C. & van Veggel, F. C. J. M. Upconverting core–shell nanocrystals with high quantum yield under low irradiance: on the role of isotropic and thick shells. *J. Appl. Phys.* **118**, 193105 (2015).

30. Ma, C. et al. Optimal sensitizer concentration in single upconversion nanocrystals. *Nano Lett.* **17**, 2858–2864 (2017).
31. Lu, Y. et al. Tunable lifetime multiplexing using luminescent nanocrystals. *Nat. Photon.* **8**, 32–36 (2013).
32. Nawa, Y. et al. Dynamic autofluorescence imaging of intracellular components inside living cells using direct electron beam excitation. *Biomed. Opt. Express* **5**, 378–386 (2014).
33. Xu, C. S. et al. Enhanced FIB-SEM systems for large-volume 3D imaging. *eLife* **3**, 1–36 (2017).
34. Zhang, Z., Kenny, S. J., Hauser, M., Li, W. & Xu, K. Ultrahigh-throughput resolved super-resolution microscopy. *Nat. Methods* **12**, 935–938 (2015).
35. DaCosta, M. V., Doughan, S., Han, Y. & Krull, U. J. Lanthanide upconversion nanoparticles and applications in bioassays and bioimaging: a review. *Anal. Chim. Acta* **832**, 1–33 (2014).
36. Denk, W. & Horstmann, H. Serial block-face scanning electron microscopy to reconstruct three-dimensional tissue nanostructure. *PLoS Biol.* **2**, e329 (2004).
37. Hayworth, K. J. et al. Ultrastructurally smooth thick partitioning and volume stitching for large-scale connectomics. *Nat. Methods* **12**, 319–322 (2015).
38. Kasthuri, N. et al. Saturated reconstruction of a volume of neocortex. *Cell* **162**, 648–661 (2015).
39. Stephenson, R. S. et al. High resolution 3-dimensional imaging of the human cardiac conduction system from microanatomy to mathematical modeling. *Sci. Rep.* **7**, 7188 (2017).
40. Angelo, M. et al. Multiplexed ion beam imaging of human breast tumors. *Nat. Med.* **20**, 436–442 (2014).

Acknowledgements

This work was supported by the Gordon and Betty Moore Foundation (grant no. 4309), the National Institutes of Health (1R01GM128089-01A1) and the National Cancer Institute CCNE-TD at Stanford University (U54CA199075). Work at the Molecular Foundry was supported by the Office of Science, Office of Basic Energy Sciences, of the US Department of Energy under contract no. DE-AC02–05CH11231. Part of this work was performed at the Stanford Nano Shared Facilities (SNSF), supported by the National Science Foundation under award ECCS-1542152. Access to the JEOL TEM 1400 was provided through the Stanford Microscopy Facility, NIH grant SIG no. 1S10RR02678001. M.B.P. was supported by the Helen Hay Whitney Foundation Postdoctoral Fellowship, and P.C.M. was supported through the Stanford Neuroscience Interdisciplinary Award. M.D.W. and J.A.D. acknowledge financial support provided as part of the DOE 'Light–Material Interactions in Energy Conversion' Energy Frontier Research Center under grant no. DE-SC0001293, as well as funding provided by the Global Climate and Energy Project at Stanford University. The authors thank N. Ginsberg and C. Aiello for providing software used in time-gated CL imaging experiments and for discussions. The authors are also grateful to J.J. Perrino and D.H. Burns for providing expertise in electron microscopy and for discussions, and R. Walsworth, D. Glenn, H. Zhang, T.C. Sudhof, J. Trotter, J. Collins and X. Zheng for discussions.

Author contributions

M.B.P., P.C.M. and S.C. conceived the project, designed experiments, analysed the data and interpreted the results. M.B.P. and P.C.M. conducted CL imaging experiments and wrote software for data analysis. M.B.P., P.C.M., A.M.C., N.L., M.D.W., C.S., B.T., G.S. and S.F. synthesized and characterized rare-earth nanoparticles. E.C. provided software for the simulation of the nanoparticle spectra. S.A., D.F.O., E.S.B. and L.-M.J. provided assistance and expertise in electron microscopy hardware and sample preparation. D.F.O. and S.A. developed the CL optics, and E.S.B. and D.F.O. developed the CL software. S.C. supervised the research. J.R., A.P.A., R.M.M., B.E.C., Y.C. and J.A.D. supervised the relevant portions of the research such as sample preparation and training M.B.P. and P.C.M. on the nanoparticle synthesis. M.B.P., P.C.M. and S.C. wrote the manuscript.

Competing interests

The authors declare no competing interests.

Additional information

Supplementary information is available for this paper at https://doi.org/10.1038/s41565-019-0395-0.

Correspondence and requests for materials should be addressed to S.C.

Methods

Nanoparticle synthesis and characterization. A series of nanoparticles were synthesized: $NaGdF_4$:Eu^{3+} and $NaGdF_4$:Er^{3+} doped at 0, 2, 5, 10, 20, 30, 50, 80 and 100%; $NaYF_4$:Eu^{3+} doped at 2, 5, 10 and 20%; $NaYF_4$:Er^{3+} doped at 5, 10 and 30%; $NaGdF_4$ nanoparticles doped with Ho^{3+}, Tb^{3+}, Sm^{3+}, Dy^{3+}, Nd^{3+}, Tm^{3+}, Ce^{3+}, Pr^{3+} and Yb^{3+} at 15%; $NaYF_4$ nanoparticles doped with Ho^{3+}, Tb^{3+}, Sm^{3+}, Dy^{3+}, Nd^{3+}, Tm^{3+}, Ce^{3+}, Pr^{3+} and Yb^{3+} at 5%. Synthesis was based on previously reported protocols[19–22] (see Supplementary Section 'Nanoparticle synthesis and characterization' for details). Briefly, 4 ml of oleic acid and 6 ml of 1-octadecene were mixed with 0.4 ml total volume (0.4 mmol) of an aqueous solution of 1 M rare-earth (RE) chloride hydrates of the desired ratios. The temperature was set to 110 °C for 40 min. Afterwards, the solution was cooled to <30 °C. Next, a nucleation precursor solution was prepared by adding 1 ml of 1 M sodium hydroxide in methanol to 4 ml of 0.4 M ammonium fluoride in methanol. After mixing, the precursor solution was vortexed for 10 s and injected into the RE–oleate mixture at room temperature under an argon atmosphere. The temperature was maintained at 50 °C under an argon atmosphere for 40 min. The temperature was further increased to 80 °C and the reaction was either exposed to air or placed under vacuum, allowing methanol to evaporate. The temperature was stabilized at 100 °C for 15 min under vacuum. Afterwards, the reaction was placed under an argon atmosphere and the temperature was increased to 300 °C ($NaYF_4$) or 320 °C ($NaGdF_4$) at a mean rate of ~15 °C min^{-1}. The growth temperature was maintained for 60 min ($NaGdF_4$) or 90 min ($NaYF_4$) before cooling the reaction to <30 °C. The samples were stored as-synthesized in oleic acid 1-octadecene. Nanoparticle characterization was carried out using TEM (Supplementary Figs. 4–7) and inductively coupled plasma mass spectrometry (Supplementary Figs. 8 and 26).

Sample preparation for single-nanoparticle CL measurements. The nanoparticles were exchanged into DMF using a modification of a published procedure[23] (see Supplementary Section 'Single-particle CL sample preparation' and Supplementary Fig. 9 for details). Briefly, 0.5–1 ml of as-synthesized nanoparticles were mixed with an equal volume of ethanol and washed by centrifugation at 3,500*g* for 3 min. The pellet was resuspended with 0.5 ml *n*-hexane and the 0.5 ml ethanol wash was repeated. The pellet was resuspended in 0.3 ml of *n*-hexane, then 0.3 ml of 11 mg ml^{-1} $NOBF_4$ in DMF was added, and the reaction was incubated for 45 min. The tube was centrifuged at 10,000*g* for 10 min and the supernatant was discarded. The pellet was washed with 0.2 ml of a 1:1 mixture of toluene and *n*-hexane at 10,000*g* for 10 min. The resulting nanoparticle pellet was dried under argon and resuspended in 0.1–0.2 ml of DMF. A 4 µl volume of nanoparticles in DMF was spin-coated on a silicon substrate to achieve a density compatible with imaging several single nanoparticles within a 1 μm^2 region.

Single-nanoparticle CL measurements. Single-nanoparticle CL measurements were carried out at the Molecular Foundry at the Lawrence Berkeley National Laboratory. Experiments were performed on a Zeiss Supra 55-VP-FESEM with a CL parabolic mirror light collection system. A 1.3π sr (1 mm focal length) diamond-turned aluminium parabolic reflector mounted on a four-axis nanopositioning stage was used to collimate the light emitted from the sample. The light was then focused onto a photomultiplier counting module (Hamamatsu H7442–40). During the measurements, the working distance was typically in the 4.9–5.2 mm range, the current was on the order of 300–500 pA and the beam energy was 5 keV. The samples were scanned using a 512×512 point grid of 1×1 µm dimensions, resulting in a pixel pitch of 1.95 nm. The dwell time per pixel was either 500 µs or 2 ms depending on the experiment and expected count rates. The estimated electron dose under these conditions was approximately 5,000–20,000 electrons $Å^{-2}$ (current density of ~100 pA nm^{-2}).

Single-nanoparticle CL data analysis. The CL intensity and SNR for individual nanoparticles were extracted by selecting a sub-region (~30×30 pixels, or ~7–8σ for $NaGdF_4$:Eu^{3+}) within the original 1 μm^2 field of view that contained one or several individual particles. Nanoparticle aggregates were avoided. The raw CL image $I(x_i, y_i)$, where x_i and y_i are discrete pixels of 1.95 nm pitch and I is measured in counts per pixel, was then fitted by a 2D Gaussian function with a linearly sloped background of the form $G(x_i, y_i) = c_0 + c_1 y_i + c_2 x_i + Ae^{\frac{-(x_i - x_0)^2 - (y_i - y_0)^2}{2\sigma^2}}$ (Supplementary Fig. 12). In the fit routine, the starting parameters for the standard deviation σ and the centre x_0 and y_0 positions were obtained from similar fits to the SE signal. The standard deviation of the CL image was constrained to not deviate by more than 10% from the SE image. The Gaussian component of the fitted function $S(x_i, y_i) = Ae^{\frac{-(x_i - x_0)^2 - (y_i - y_0)^2}{2\sigma^2}}$ represents the CL signal of an individual nanoparticle. The sum of $S(x_i, y_i)$ corresponds to the number of counts associated with each nanoparticle. Note, since the 'counts' are derived from a fitted function, the sum is generally not an integer. The SNR was calculated by first summing the CL signal of the nanoparticle $S_{total} = \sum_i S(x_i, y_i)$, including only the pixels in which the signal is greater than a defined threshold, which is commonly taken as the signal at pixels 2σ (95% confidence level) away from the centre of the Gaussian distribution. The threshold of 2σ was used because it is ideal when the background level is equal to the amplitude of the Gaussian of the fitted CL signal, which is the case for the data collected in this work. The noise was calculated for the same pixels as $N_i = \sqrt{G(x_i, y_i)}$ and the total noise was determined by adding the noise for each pixel in quadrature: $N_{total} = \sqrt{\sum_i N_i^2}$. The overall SNR for a single nanoparticle was then defined as the ratio $\mathrm{SNR} = \frac{S_{total}}{N_{total}}$. The nanoparticle SEM FWHM was calculated from the standard deviation, σ, as $\mathrm{FWHM} = 2\sigma\sqrt{2\ln 2} = 2.35\sigma$. Note that in this analysis the CL signal is approximated by a Gaussian function, and does not include such imaging artefacts as astigmatism, sample drift or charging.

Ensemble CL measurements. A 0.5 ml volume of as-synthesized nanoparticle solution in oleic acid and 1-octadecene was washed three times with 0.5 ml ethanol at 3.5*g* for 3 min at room temperature. The nanoparticles were redispersed in *n*-hexane and dropcast repeatedly on a ~5×5 mm^2 piece of silicon wafer until an opaque white film of nanoparticles was visible by eye. Nanoparticle spectra were measured with a JEOL JXA-8230 SuperProbe electron microscope equipped with an xCLent III hyperspectral CL system. See Supplementary Section 'Ensemble spectral measurements and sample preparation' for further details.

Simulations of nanoparticle spectra. The luminescence spectra for different dopants (Eu^{3+}, Er^{3+}, Ho^{3+}, Tb^{3+}, Sm^{3+}, Dy^{3+}, Nd^{3+}, Tm^{3+} and Yb^{3+}) were qualitatively estimated using Judd–Ofelt theory[26,27]. A rate-equation-based model, which incorporates electric and magnetic dipole transitions, cross relaxations between multiple rare-earth ions and multi-phonon relaxations in the host lattice, was used (for more details on the software package see ref. [28]). Although electron excitation generally involves high-lying energy states, which cannot be described by Judd–Ofelt theory, emission in the visible spectrum can be accurately modelled. The present Judd–Ofelt simulations were restricted to energy levels below 25,000 cm^{-1}.

Data availability

The data sets generated during and/or analysed during the current study are available from the corresponding author on reasonable request.